Optik - International Journal for Light and Electron Optics 246 (2021) 167836

Contents lists available at ScienceDirect

Optik

journal homepage: www.elsevier.com/locate/ijleo

Promising computational, structural, vibrational and optical properties of piperazinium bis(2-carboxypyridine)monohydrate (PBCPM) crystal for NLO device applications

K. Aswaniya [a,b], M.B. Jessie Raj [b,*], S. Gowri [a], G. Vinitha [c]

[a] Department of Physics, Cauvery College for Women(A) (Affiliated to Bharathidasan University, Tiruchirappalli), Tiruchirappalli 620 018, Tamil Nadu, India

[b] PG and Research Department of Physics, Bishop Heber College (A) (Affiliated to Bharathidasan University, Tiruchirappalli), Tiruchirappalli 620 017, Tamil Nadu, India

[c] Division of Physics, School of Advanced Sciences, Vellore Institute of Technology (VIT), Chennai 600 127, India

ARTICLE INFO

Keywords:
Single-crystal XRD
DFT
Hirshfeld
Hyperpolarizability
FT-IR
FT-Raman
NLO

ABSTRACT

The Slow Evaporation Solution Technique (SEST) was used to produce a single crystal of piperazinium bis(2-carboxypyridine)monohydrate (PBCPM). The lattice parameters and molecular structure of the grown crystal were determined using Single Crystal X-Ray Diffraction. The intramolecular and intermolecular interactions were visualised using Hirshfeld surface analysis. The B3LYP level of theory with a 6–31++G (d,p) basis set was used to compute the Molecular optimised geometry. The FT-IR and FT-R spectral studies that have been reported look at the modes of vibration of various functional groups in the PBCPM crystal. The grown crystal has a high transmittance in the entire visible field, according to UV–vis transmittance reports. Based on the finite-field approach, the polarizability and hyperpolarizability of PBCPM is determined using the DFT-B3LYP method and the 6–311G(d,p) basis set. The Z-scan technique is used to perform third order NLO studies on the PBCPM crystal. The result discussed confirms that PBCPM crystal is a potential candidate for future NLO device applications.

1. Introduction

The widespread use of high-power lasers in various applications has drew a lot of attention to nonlinear optical (NLO) materials in recent years. Researchers have been working hard to develop and synthesised high-quality NLO materials in recent years due to their use in frequency transfer, optical information processing, optoelectronic switches, photonics, telecommunication, and optical data storage [1–4]. Organic materials have a wide range of properties. Organic materials have the advantage of allowing consumers to change the chemical composition with a wide range of physical dimensional diversity and properties for the ideal NLO properties [5,6]. The fact that the Second-harmonic generation (SHG) property is closely associated with a non-centrosymmetric crystalline structure has been well-confirmed by theoretical and experimental analysis.

According to the Kleinman approximation, $\chi^{(2)}$ has no independent irreducible part of tensor in the centrosymmetric crystal due to symmetry property, thus exhibiting no SHG effect [7]. However, several studies have shown that centrosymmetric crystals have SHG

* Corresponding author.
E-mail address: jessie.ph@bhc.edu.in (M.B.J. Raj).

https://doi.org/10.1016/j.ijleo.2021.167836
Received 18 July 2021; Accepted 13 August 2021
Available online 16 August 2021

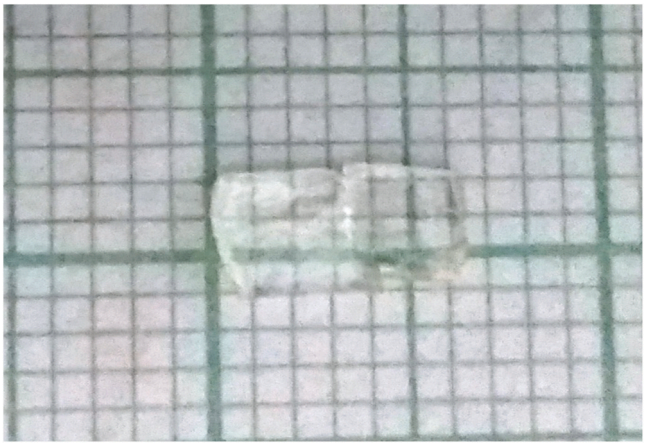

Fig. 1. Grown crystal of PBCPM by solvent evaporation method.

properties [8].

The density and anisotropy of SHG are caused by surface electric dipoles and bulk electric quadruple in centrosymmetric crystals, according to Lüpker's phenomenological theory. The centrosymmetric system's surface-sensitive SHG changes with surface oxidisation, allowing surface contribution to SHG to be identified [9]. Primitive to materials with disappearing $\chi^{(2)}$[10], approximately 75% of all organic molecules crystallise in centrosymmetric space groups. Piperazine and its derivatives have been studied widely in a variety of areas, including complexant agents, pharmaceutical products, and biologic substances for some metabolic processes [11]. Because of their electrical, mechanical, and magnetism properties, these materials have piqued scientists' interest and sparked a lot of research. For vibrational investigations and H-bond interactions, crystals containing piperazine cation were extensively studied [12–15]. Piperazinium 4-nitrophenolate monohydrate [16], piperazinium mesotartrate [17], and phosphoric acid pyridine-1-ium-2-carboxylate [18] have all recently been discovered to be possible third-order NLO materials. The existence of H-bond interactions in these materials has a significant impact on the Non-Linear Optical behaviour. Picolinic acid, by means of its acidic composition, crystallises with a variety of organic molecules and forms salts by complex electrostatic or H-bonding interactions. NLO materials include picolinic acid hydrochloride [19] and picolinic acid co-crystallized with dicarboxylic acids [20] crystals. The growth, single-crystal X-ray diffraction, Hirshfeld surface analysis, Molecular geometry, Z-Scan measurement, FT-IR, FT-Raman, frontier molecular orbital using the TD-DFT process, and hyperpolarisability measurements of the PBCPM crystal are all discussed in this paper. The experimental and theoretical findings are consistent, and the measurements reveal information about the vibrational spectra and molecular properties.

2. Experimental

Piperazine and Picolinic Acid were used as source materials to expand a single crystal of PBCPM using a slow evaporation technique. As a solvent, double distilled water was used. Piperazine and Picolinic Acid is dissolved in a 1:1 ratio in 10 mL of double distilled water. The solution was constantly mixed well with a magnetic stirrer at room temperature for around three hours to achieve a homogeneous mixture. The solution was then purified to eliminate immiscible impurities using Whatman filter paper before being allowed to evaporate. The purity of the grown crystal is improved by the recrystallization process. Over the course of 45 days, optically good single crystals were harvested, which is one of the prerequisite for optoelectronic device fabrication. Fig. 1 depicts a photographic image of a PBCPM grown crystal.

3. Characterization details

A Bruker APEX II single crystal diffractometer with CuKα radiation ($\lambda = 0.71073$Å) was used to collect crystallographic data. The Perkin-Elmer Spectrometer was used to record the Fourier Transform Infrared (FT-IR) spectrum of KBr pellet in the frequency range of 400–4000 cm^{-1}. A BRUKER RFS 27: Standalone FT-Raman Spectrometer was used to capture the Fourier Transform Raman (FT-Raman) spectrum. Perkin Elmer Model: Lambda 35 was used to study the UV-Vis-NIR spectrum of PBCPM crystal in the wavelength range 190–1100 nm.

4. Computational details

SAINT [21] was used to reduce the amount of data and optimise the cells of the crystal structure. SHELXS-97 [22] was used to solve the crystal structure directly, and SHELXL-97 [23] was used to refine the data using complete matrix least square fitting. The structure was examined with PLATON [24,25], and there were no solvent-accessible voids in the crystal lattice. Further Hirshfeld surface analysis was performed using the program CrystalExplorer [26]. The Becke3–Lee–Yang–Parr (B3LYP) functional was supplemented

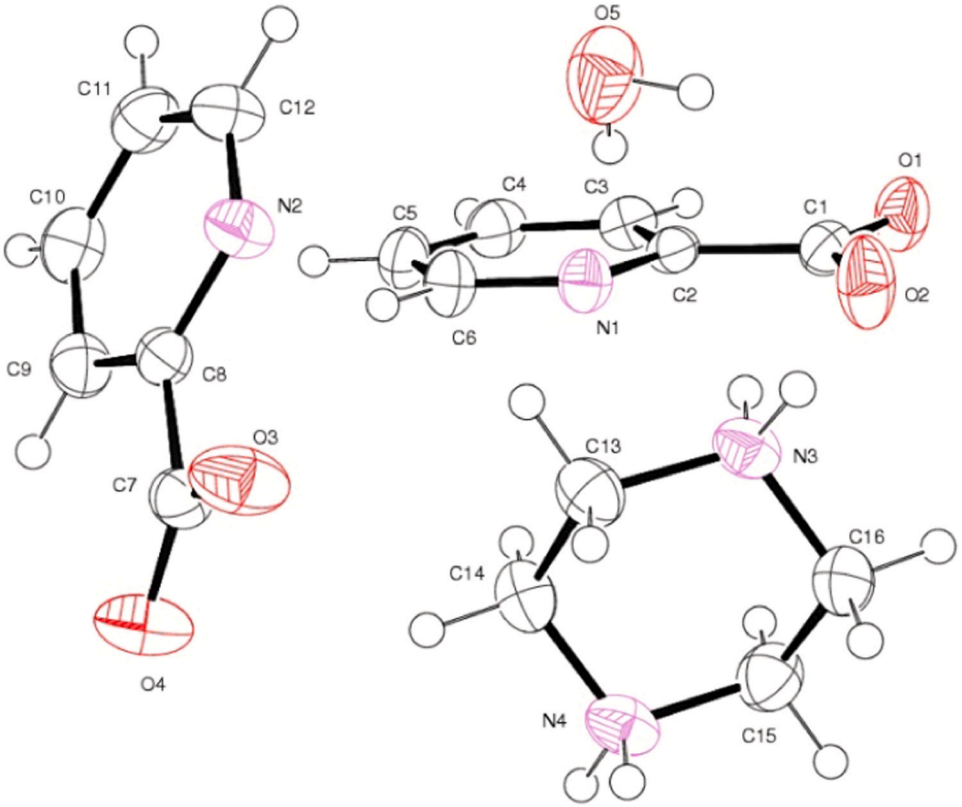

Fig. 2. ORTEP diagram of PBCPM.

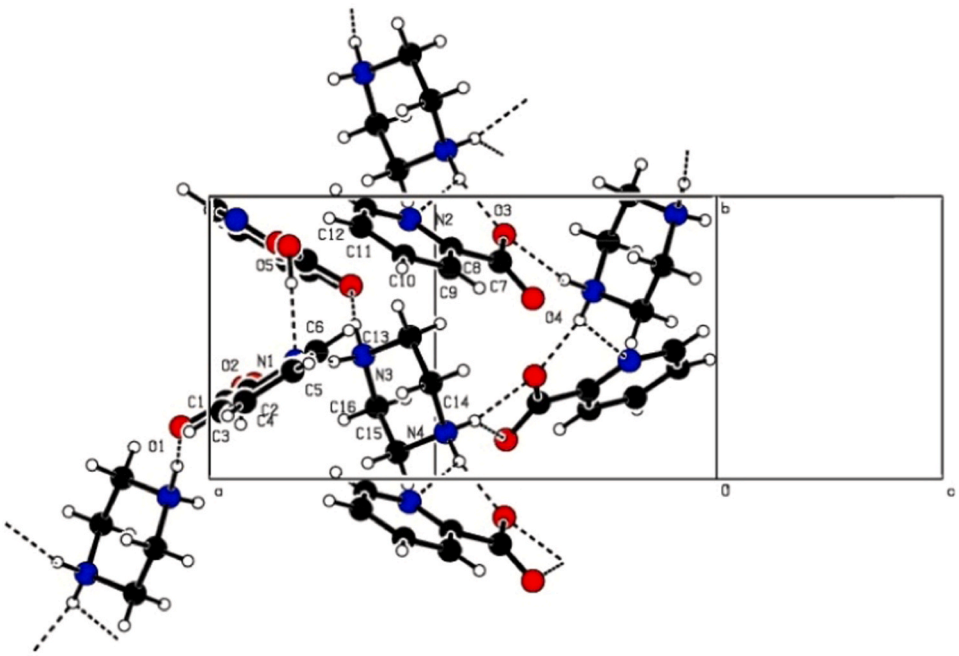

Fig. 3. Hydrogen bonding of PBCPM.

Table 1
Crystal data and structure refinement data of PBCPM.

Empirical formula	$C_{16}H_{22}N_4O_5$
Formula weight	350.37
Temperature	296(2) K
Wavelength	0.71073 Å
Crystal system	Monoclinic
Space group	P21/c
Unit cell dimensions	a = 12.4458(3), b = 6.7904(2) c = 19.8785(5) Å β = 94.3964(15)
Volume	1675.03(8) Å3
Z	4
Density (calculated)	1.389 Mg/m3
Absorption coefficient	0.11 mm-1
Index ranges	-10 < = h < = 10, − 10 < = k < = 8, − 16 < = l < = 15
Reflections collected	12,606
Independent reflections	2933[R(int) = 0.023]
Data / restraints / parameters	2933/ 0 / 250
Goodness-of-fit on F2	1.09
Final R indices [I>2sigma(I)]	R1 = 0.036, wR2 = 0.098

Table 2
Hydrogen bond geometry of PBCPM.

Hydrogen-bond geometry (Å, °)				
D—H···*A*	*D*—H	H···*A*	*D*···*A*	*D*—H···*A*
O5—H1*O*···N1	0.93 (3)	2.13 (3)	3.051 (2)	169 (3)
O5—H2*O*···O2i	0.93 (3)	1.82 (3)	2.7451 (17)	168 (2)
N4—H4*N*···O4ii	0.94 (2)	2.31 (2)	3.0853 (18)	138.7 (17)
N4—H4*N*···O3ii	0.94 (2)	1.94 (2)	2.8379 (17)	159.0 (18)
N3—H2*N*···O1i	1.03 (2)	1.68 (2)	2.6825 (17)	165.2 (17)
N4—H3*N*···O3iii	0.96 (2)	1.81 (2)	2.7108 (18)	156.9 (17)
N4—H3*N*···N2iii	0.96 (2)	2.48 (2)	3.1378 (18)	125.8 (14)
N3—H1*N*···O2	0.858 (18)	1.996 (18)	2.7399 (18)	144.4 (15)
N3—H1*N*···N1	0.858 (18)	2.521 (18)	3.2531 (18)	143.8 (14)
C16—H16*A*···O4ii	0.97	2.65	3.369 (2)	132
C15—H15*A*···O5iii	0.97	2.58	3.472 (2)	153
O5—H1*O*···N1	0.93 (3)	2.13 (3)	3.051 (2)	169 (3)
O5—H2*O*···O2i	0.93 (3)	1.82 (3)	2.7451 (17)	168 (2)
N4—H4*N*···O4ii	0.94 (2)	2.31 (2)	3.0853 (18)	138.7 (17)
N4—H4*N*···O3ii	0.94 (2)	1.94 (2)	2.8379 (17)	159.0 (18)
N3—H2*N*···O1i	1.03 (2)	1.68 (2)	2.6825 (17)	165.2 (17)
N4—H3*N*···O3iii	0.96 (2)	1.81 (2)	2.7108 (18)	156.9 (17)
N4—H3*N*···N2iii	0.96 (2)	2.48 (2)	3.1378 (18)	125.8 (14)
N3—H1*N*···O2	0.858 (18)	1.996 (18)	2.7399 (18)	144.4 (15)
N3—H1*N*···N1	0.858 (18)	2.521 (18)	3.2531 (18)	143.8 (14)
C16—H16*A*···O4ii	0.97	2.65	3.369 (2)	132
C15—H15*A*···O5iii	0.97	2.58	3.472 (2)	153
C15—H15*A*···O5iii	0.97	2.58	3.472 (2)	153
C16—H16*A*···O4ii	0.97	2.65	3.369 (2)	132
N3—H1*N*···N1	0.858 (18)	2.521 (18)	3.2531 (18)	143.8 (14)
N3—H1*N*···O2	0.858 (18)	1.996 (18)	2.7399 (18)	144.4 (15)
N4—H3*N*···N2iii	0.96 (2)	2.48 (2)	3.1378 (18)	125.8 (14)
N4—H3*N*···O3iii	0.96 (2)	1.81 (2)	2.7108 (18)	156.9 (17)
N3—H2*N*···O1i	1.03 (2)	1.68 (2)	2.6825 (17)	165.2 (17)
N4—H4*N*···O3ii	0.94 (2)	1.94 (2)	2.8379 (17)	159.0 (18)
N4—H4*N*···O4ii	0.94 (2)	2.31 (2)	3.0853 (18)	138.7 (17)
O5—H2*O*···O2i	0.93 (3)	1.82 (3)	2.7451 (17)	168 (2)
O5—H1*O*···N1	0.93 (3)	2.13 (3)	3.051 (2)	169 (3)

Symmetry codes: (i) −x + 2, y + 1/2, −z + 1/2; (ii) −x + 1, y − 1/2, −z + 1/2; (iii) x, y − 1, z.

Table 3
Optimized Geometry of PBCPM.

Bond Length	Exp. (Å)	Theoretical (Å)	Bond Length	Exp. (Å)	Theoretical (Å)
C1—O2	1.244(18)	1.321	C12—N2	1.335(19)	1.319
C1—O1	1.245(18)	1.1855	C13—N3	1.478(2)	1.4491
C1—C2	1.515(2)	1.5056	C13—C14	1.508(2)	1.5207
C2—N1	1.342(18)	1.3549	C14—N4	1.474(2)	1.4789
C2—C3	1.380(2)	1.3791	C15—N4	1.476(2)	1.4822
C3—C4	1.377(2)	1.3874	C15—C16	1.501(2)	1.5188
C4—C5	1.376(2)	1.3806	C16—N3	1.484(2)	1.4507
C5—C6	1.374(2)	1.3902	C8—N2	1.339(19)	1.3239
C6—N1	1.336(19)	1.3211	C8—C9	1.380(2)	1.3884
C7—O4	1.234(19)	1.2443	C9—C10	1.381(2)	1.3826
C7—O3	1.259(18)	1.2329	C10—C11	1.371(2)	1.3827
C7—C8	1.515(2)	1.5235	C11—C12	1.376(2)	1.3847
Bond Angle	**Exp.(°)**	**Theoretical(Å)**	**Bond Angle**	**Exp.(°)**	**Theoretical(Å)**
O2—C1—O1	125.67(14)	122.74	N4—C14—C13	110.63(13)	110.0883
O2—C1—C2	116.94(13)	114.12	N4—C15—C16	109.95(14)	109.8885
O1—C1—C2	117.38(13)	123.12	N3—C16—C15	111.43(13)	108.8456
N1—C2—C3	122.13(14)	123.8068	C6—N1—C2	117.31(13)	118.8777
N1—C2—C1	116.65(12)	115.5901	C12—N2—C8	116.92(13)	118.3741
C3—C2—C1	121.22(13)	120.6026	C13—N3—C16	112.09(12)	112.4723
C4—C3—C2	119.50(14)	117.4137	C14—N4—C15	110.81(12)	113.0378
C5—C4—C3	118.83(14)	119.0478	C11—C10—C9	118.71(15)	118.733
C6—C5—C4	118.21(14)	119.0982	C10—C11—C12	118.52(15)	118.0022
N1—C6—C5	124.02(15)	121.7555	N2—C8—C9	122.77(13)	122.5379
O4—C7—O3	124.09(14)	126.3101	N2—C8—C7	116.58(12)	118.2959
O4—C7—C8	118.19(14)	117.1819	C9—C8—C7	120.64(13)	119.1662
O3—C7—C8	117.69(13)	116.5078	C8—C9—C10	119.12(15)	118.7361
N2—C12—C11	123.96(15)	123.6158	N3—C13—C14	111.44(13)	109.0053
Torsional Angle	**Exp.(°)**	**Theoretical(Å)**	**Torsional Angle**	**Exp.(°)**	**Theoretical(Å)**
O2—C1—C2—N1	3.2(2)	-3.4476	C8—C9—C10—C11	0.6(2)	0.1353
O1—C1—C2—N1	− 176.52(13)	176.3014	C9—C10—C11—C12	− 0.3(2)	0.093
O2—C1—C2—C3	− 176.48(15)	176.8119	C10—C11—C12—N2	− 0.7(3)	-0.1362
O1—C1—C2—C3	3.8 (2)	-3.4391	N3—C13—C14—N4	54.76(17)	55.4715
N1—C2—C3—C4	− 0.9(2)	0.1301	N4—C15—C16—N3	− 56.35(17)	-56.1043
C1—C2—C3—C4	178.76(13)	179.8485	C5—C6—N1—C2	0.5(2)	-0.1364
C2—C3—C4—C5	1.0(2)	-0.197	C3—C2—N1—C6	0.1(2)	0.0376
C3—C4—C5—C6	− 0.4(2)	0.1077	C1—C2—N1—C6	− 179.51(13)	-179.6936
C4—C5—C6—N1	− 0.3(3)	0.0636	C11—C12—N2—C8	1.3(2)	-0.0666
O4—C7—C8—N2	− 163.79(14)	4.7548	C9—C8—N2—C12	− 1.0(2)	0.3155
O3—C7—C8—N2	14.3(2)	-175.1056	C7—C8—N2—C12	177.96(14)	-179.6025
O4—C7—C8—C9	15.2(2)	-175.1661	C14—C13—N3—C16	− 52.48(17)	-61.3884
O3—C7—C8—C9	− 166.79(14)	4.9735	C15—C16—N3—C13	53.56(18)	61.7724
N2—C8—C9—C10	0.0(2)	-0.3529	C13—C14—N4—C15	− 58.44(17)	-53.8465
C7—C8—C9—C10	− 178.85(14)	179.5645	C16—C15—N4—C14	59.16(17)	54.2012

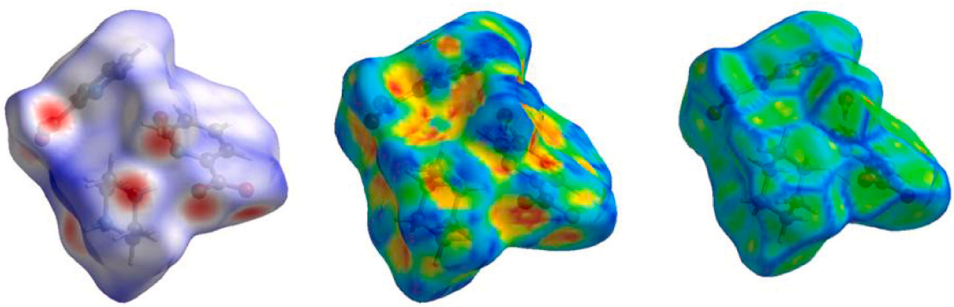

Fig. 4. dnorm, shapeindex, curvedness of PBCPM crystal.

with the standard B3LYP/6–31++g(d,p) basis set [27] to find the optimised geometry, Hyperpolarizability, HOMO–LUMO with Gaussian-09W [28] software using the Becke3–Lee–Yang–Parr (B3LYP) functional supplemented with the standard B3LYP/6–31++g (d,p). To create visual displays and check the standard mode assignments, the Gauss view 05 software [29] was used.

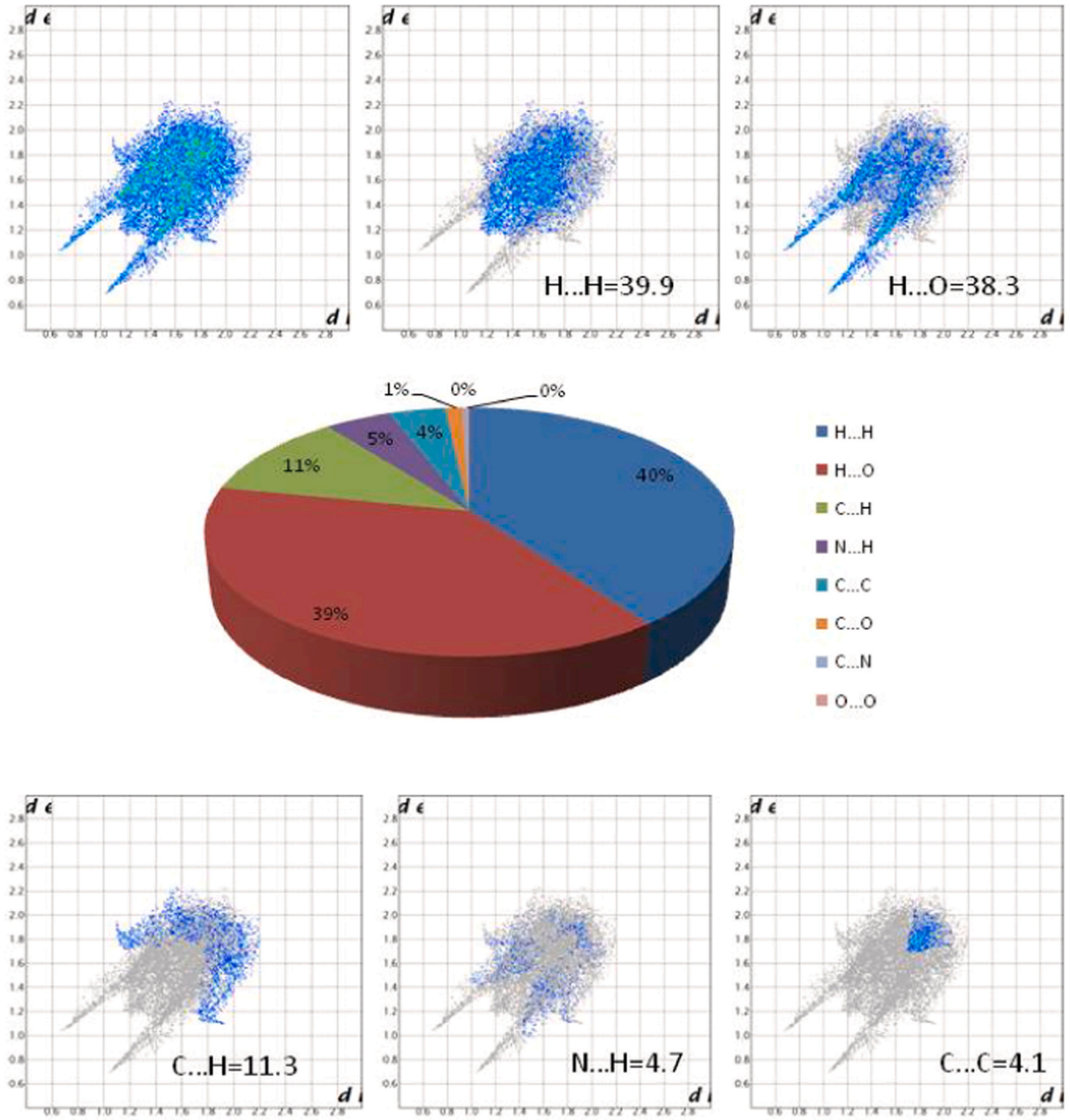

Fig. 5. 2D fingerprint plot of PBCPM.

5. Result and discussion

5.1. Single crystal X-ray diffraction studies

The identification of cell parameters and efficiency was confirmed using a single crystal X-ray Diffraction analysis on a grown crystal of PBCPM [22,23]. Cell parameters are observed to be a = 12.4458(3)Å, b = 6.7904(2)Å, c = 19.8785(5)Å and efficiency is 94.3964(15)°, with a cell volume of 1675.03(8)Å^3. The R_{int} factor, also known as the difference index, of the PBCPM crystal is 0.036, indicating that the crystallographic model and experimental X-ray diffraction results are in agreement. The grown crystal has the space group P21/c and is monoclinic. Fig. 2 depicts the ORTEP diagram of the PBCPM compound. PBCPM crystal has a Z value of 4. PBCPM crystal has a Goodness of Fit (S) rating of 1.09. Fig. 3 depicts the hydrogen bonding of PBCPM. at the 50% probability range, with displacement ellipsoids plotted The total number of measured reflections is 12,606, with 2933 individual reflections. Table 1 and Table 2 show the crystal data and structure refinement data of PBCPM, as well as the hydrogen bond geometry of PBCPM [24] Table 3

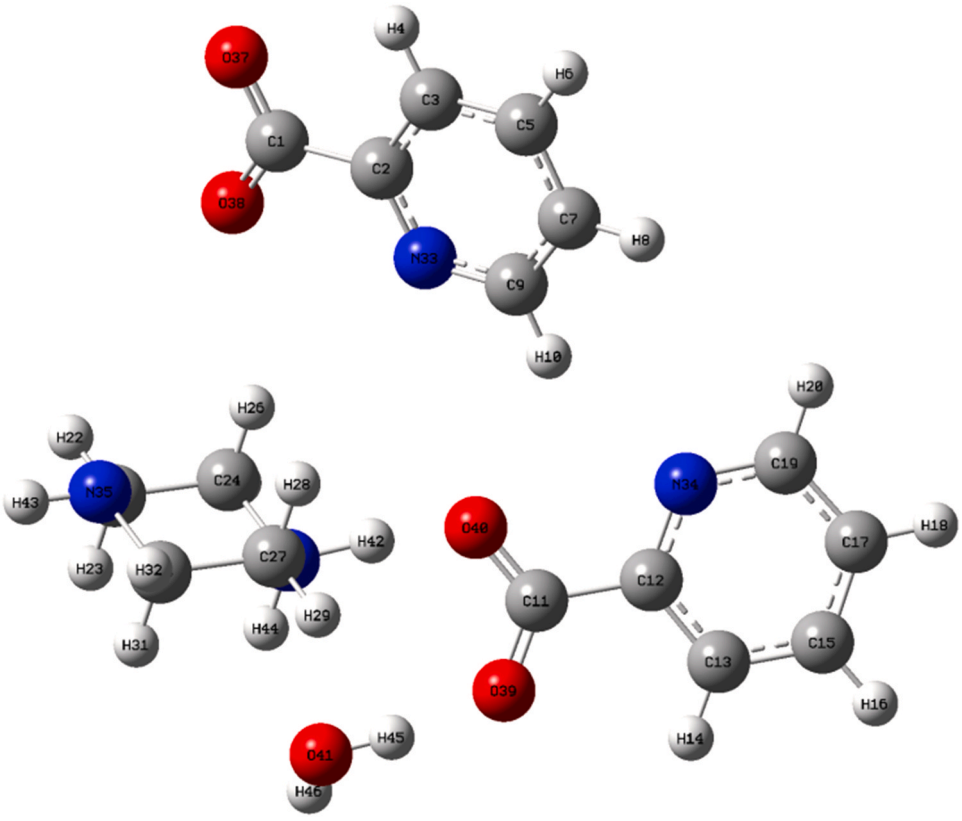

Fig. 6. Optimized Structure of PBCPM.

lists the chosen bond length and bond angles for both experimental and theoretical values[25]. The CCDC number of the PBCPM is 2031235.

5.2. Hirshfeld surface analysis

For a greater understanding of the crystallographic force guiding the molecular configuration and packing nature of the molecule in their crystal structure, Hirshfeld surface analysis is used [30,31]. Fig. 4 shows the d_{norm}, shape index and curvedness of molecular Hirshfeld surface analysis for synthesised PBCPM crystal, which are mapped over dnorm ranges of − 0.705–1.449 Å, shape index ranges of − 1.0000–1.0000 Å, and curvedness ranges of − 4.0000–0.4000 Å, respectively. Intermolecular interactions such as H.H, H.O, C.H, N.H, and C.C are well dominated on the Hirshfeld graphical surfaces, according to the 2D fingerprint plots. Fig. 5 shows the percentage contribution of chosen interatomic contacts to the Hirshfeld surface region for PBCPM, as well as a 2D fingerprint map of PBCPM. The contribution of H.H (39.9%), H.O (38.3%), C.H (11.3%), N.H (4.7%), and C.C (4.1%) intermolecular interactions, which have constituted the complete Hirshfeld surface, is thoroughly examined using the maximum 2D fingerprint plots. The intermolecular interactions H.H and H.O have covered 39.9% and 38.3% of the molecule's gross Hirshfeld surface area, respectively. Close-contact interactions are primarily responsible for the major intermolecular hydrogen bonding interactions, as shown by the deep red spots on the d_{norm} Hirshfeld surfaces.

5.3. Molecular geometrical analysis

Fig. 6 shows the optimised PBCPM structures obtained at the B3LYP/6–31 + +g(d,p) stage. PBCPM experimental X-Ray diffraction values are in good agreement with the measured bond angles, bond lengths, and dihedral angles. Table 3 lists the PBCPM's optimized structural parameters. The estimation of geometric parameters is successful, according to Foresman and Frisch, if the variance of bond length between the measured and experimental value is approximately 0.01–0.02 and the deviation of bond angle and torsion angle is approximately 1–2° [27,32]. The C—C bond has an average bond length of 1.412 Å (Experimental) and 1.420 Å (calculated). The C—C bond experiences a divergence of 0.0074. The mean difference between experimental and theoretical C1-O2 bond length is 0.0766 Å, while the minimum difference in C3-C3 bond length is 0.0009 Å. Bond angles O2-C1-O1 and C11-C10-C9 have maximal and minimum deviations of 2.93 and 0.023º, respectively. The majority of the dihedral angle agrees well with the X-ray diffraction values.

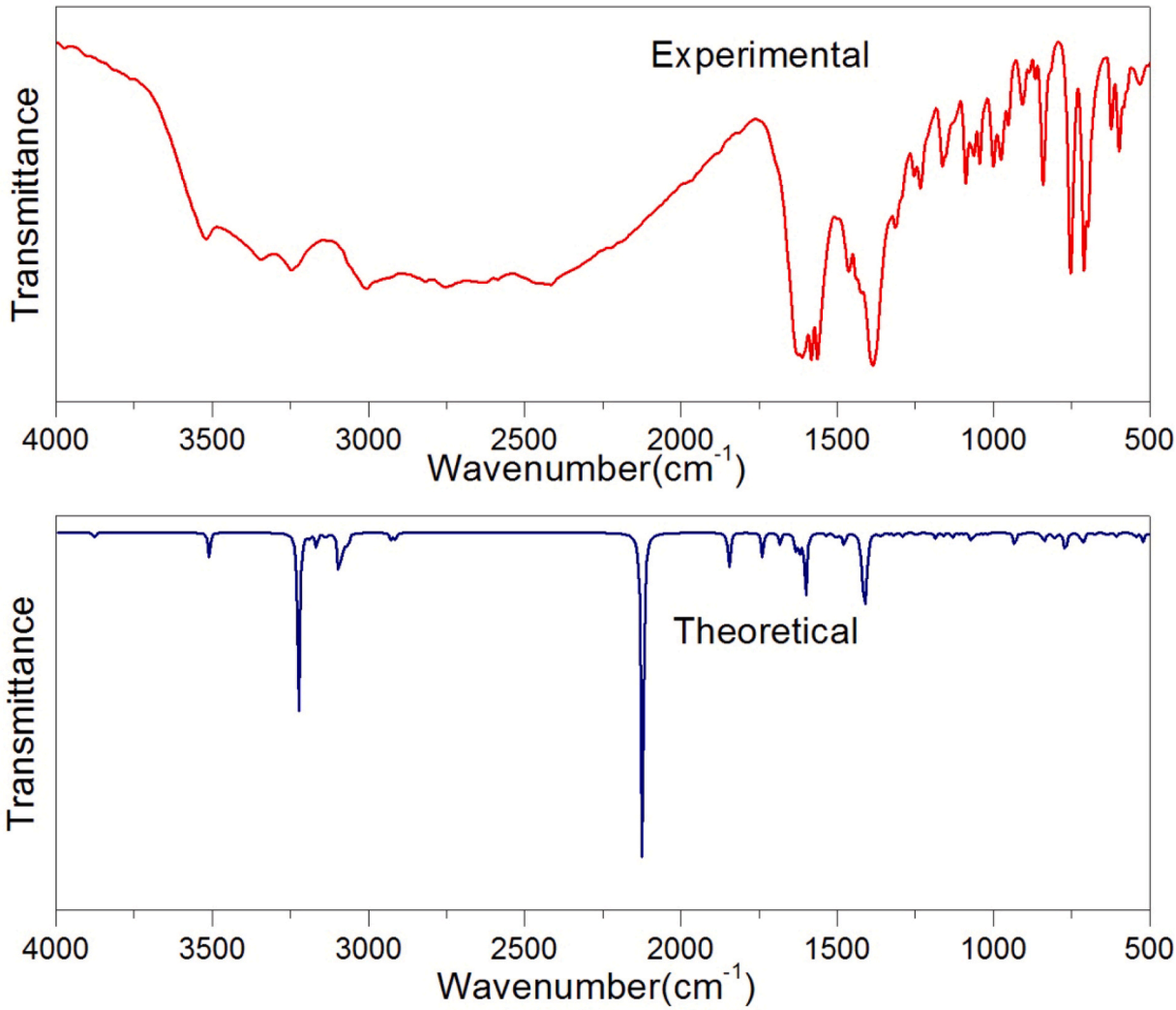

Fig. 7. Experimental and Theoretical FT-IR spectrum of PBCPM.

5.4. *Vibrational assignments*

The Experimental and Theoretical FT-IR and FT-Raman spectrum clearly predicts the vibrational bands of the grown PBCPM, shown in Figs. 7 and 8.

5.4.1. *O—H vibrations*

Due to O—H stretching and bending vibrations, water molecules integrated into the lattice framework of a crystalline compound create distinctive bands in the range of 3800–3200 cm^{-1} and 1700–1600 cm^{-1}. The O—H vibration is allocated to the bands at 3759 cm^{-1} in the experimental FT-Raman of PBCPM crystal in this study. Table 4 shows how the B3LYP level at 6–31++G(d, p) gives the wavenumber value of 3764 cm^{-1} for O—H vibrations [27].

5.4.2. *N—H vibration*

The N—H stretching vibrations occur in the range 3500–3300 cm^{-1} in all heterocyclic compounds. The N—H vibrates at 3441 cm^{-1} in the experimental FT-Raman spectrum and 3441 cm^{-1} in the theoretical spectrum in this study.

5.4.3. *C—H vibrations*

Due to aromatic C—H stretching vibrations, aromatic compounds typically exhibit several weak bands in the range of 3100–2900 cm^{-1}. C—H stretching can be assigned to the band seen at 3067, 3005, and 2820 cm^{-1} in the FT-Raman spectrum and an extreme band seen at 3067, 3005, and 2824 cm^{-1} in the FT-IR spectrum.

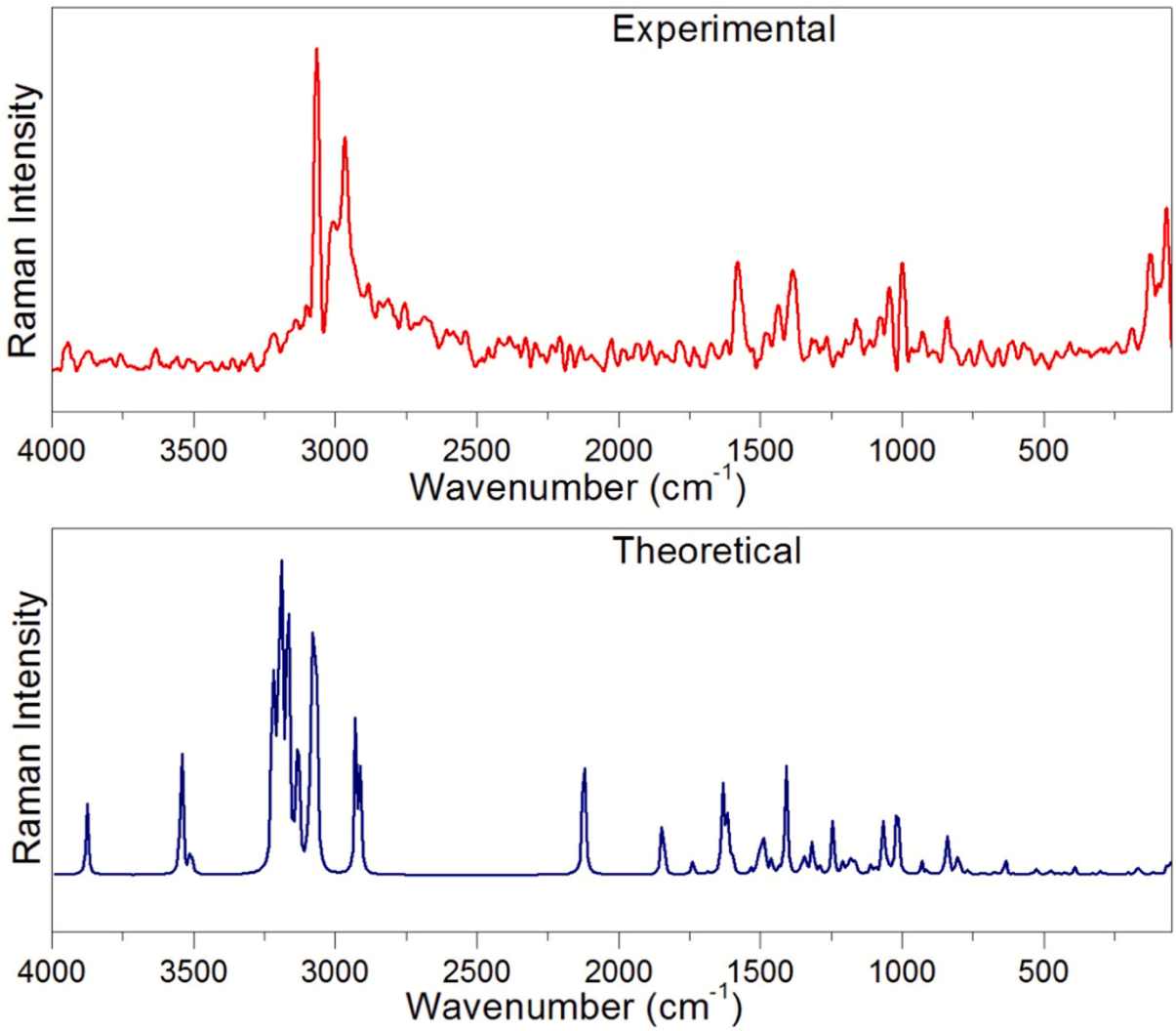

Fig. 8. Experimental and Theoretical FT-Raman spectrum of PBCPM.

5.4.4. C—N vibrations

C—N stretching bands can be seen in all amines, with aromatic amines showing bands in the 1360–1250 cm^{-1} range and aliphatic amines showing bands in the 1220–1020 cm^{-1} range. As a result, the C—N stretching mode of vibrations is applied to the FT-IR bands observed at 1318 & 1295 cm^{-1} and the bands observed at 1317 & 1287 cm^{-1} in the FT-Raman spectrum of PBCPM in this study. The C—N stretching vibrations have band positions of 1316 and 1295 cm^{-1} in the measured bands at the B3LYP level in the same region [27].

5.4.5. Root mean square error

Fig. 9 shows the Root Mean Square Error plot, with the Root Mean Square Error value of 4.67cm1. By adding the squares of the differences between the observed and measured frequencies, dividing by the number of deviations, and taking the square root, the RMSE value can be calculated.

5.5. CHNS/O elemental analysis

The PBCPM crystal was subjected to a CHNS/O elemental analysis using a Perkin-Elmer Series II 2400 CHNS/O Elemental Analyzer. The elemental analysis revealed that the crystal's composition (in weight percent) is as follows: N: 16.02, O: 22.88). C: 54.98, H: 6.04, N: 16.02, O: 22.88). When both are added together, the resulting value is 99.92 wt%. The determined values are in accordance with the microanalysis of the grown PBCPM crystalline material (C: 55.00, H: 6.06, N: 16.04, O: 22.90) The estimated worth of 100 wt % as a result indicates the crystalline quality of the prepared PBCPM is without any impurity.

Table 4
Theoretical and Experimental vibrational wavenumbers (cm^{-1}) of PBCPM crystal calculated by B3LYP/6–31++G(d,p).

S.No	FT-Raman	FT-IR	Theo. Freq.	IR Intensity	Raman Activity	Potential Energy Distribution (%)
1	–	–	12.8608	0.4775	1.9921	βNHO(12) + βNHC(14) + τNHCC(16) + τNCOH(13)
2	–	–	17.5099	0.9436	1.0364	τNHCC(15) + τCNHC(18) + τCNHC(23)
3	–	–	21.6055	2.1993	2.4014	βNHO(10) + βNHC(14) + τHOHN(19)
4	–	–	29.1947	1.8553	1.183	υNH(14) + βNHC(32) + τCNHC(10)
5	–	–	30.4861	3.4312	2.5784	βNHO(13) + τNHCC(17)
6	–	–	36.9851	0.2582	2.2935	υNH(26) + τHOHN(13) + τHOCO(12) + γNCOH(12)
7	–	–	40.9685	0.4257	0.5213	υNH(31) + τOCCN(17)
8	–	–	51.3623	3.175	6.016	τNHCC(12) + τCNHC(18) + τCCNH(27) + τCNHC(10)
9	–	–	55.0475	3.2479	1.1788	τOCCN(28)
10	–	–	61.1963	0.6428	0.2971	τHOCO(21)
11	68	–	64.834	2.5023	4.0029	βHOC(12) + βNHC(10) + βCNH(21)
12	95	–	95.593	10.9681	0.3808	βHOC(10) + βHOC(21) + βCNH(14)
13	–	–	98.1587	4.0241	0.4282	βCNH(20) + τHOHN(26) + τOCCC(10)
14	–	–	113.9475	2.1922	0.8236	τOCCC(68)
15	122	–	123.1063	20.2337	0.4448	υOH(25) + βOCC(19)
16	–	–	160.9623	0.2267	2.9274	τCCCN(22) + γOCOC(11) + γCCNC(53)
17	–	–	169.9983	1.171	3.5767	τCNHC(17) + τCCCN(16) + τCCNH(17) + γCNCC(17)
18	191	–	200.0229	16.7901	0.9721	υOH(50) + βHOC(12)
19	–	–	211.1992	30.0787	0.1123	βHOC(14) + βOCH(21)
20	–	–	223.6943	13.6681	0.3323	βOCC(28) + βCCN(56)
21	248	–	259.0292	9.1507	0.2162	τNCCN(37)
22	–	–	281.7838	40.0161	0.6454	βHOC(12) + βHOH(12) + βCCC(24)
23	293	–	298.8769	49.9858	2.5716	βHOH(39) + βCCC(15)
24	316	–	329.0293	11.056	0.6965	βCNC(10) + βHOH(11) + βOCH(14) + τCNCC(11)
25	376	–	391.7003	0.6524	3.8885	υCC(41) + βOCO(21)
26	407	–	417.2553	2.235	0.1479	τHCCC(11) + τHCCC(12) + τCCCC(32) + τCCCN(18)
27	–	–	423.0492	9.9771	0.6887	βCNC(21)
28	–	–	423.8026	2.0221	0.1364	τCNCC(19) + τCCCN(26) + τCCCC(17)
29	419	418	426.5879	24.7226	0.4172	υCC(21)
30	–	–	448.5177	0.595	0.5195	τHCCC(10) + τCNCC(18) + τCCCN(18) + τCCCC(16) + γOCOC(10)
31	–	–	454.5868	1.1538	0.2744	τCCCN(19) + γCNCC(28)
32	458	–	473.993	3.8031	2.0944	βNCC(22) + βCCN(16)
33	–	469	484.5344	130.0627	1.8424	υOH(14)
34	505	503	520.6337	75.9161	1.3646	βHOH(18) + τHOHN(27) + τHOCO(15) + γOCOH(10)
35	–	–	528.1647	5.7846	2.7936	βOCC(52) + βCCN(20)
36	526	531	543.9171	43.9106	0.3058	βOCC(44) + βCCC(11)
37	–	583	606.1717	41.618	0.4182	βCNC(18)
38	–	–	635.5542	12.2801	4.8403	βCCC(19) + βCCN(35)
39	624	623	637.904	6.9181	5.3678	βCNC(24) + βCCC(22) + βCCC(10)
40	659	–	674.8061	12.8015	2.4105	βOCO(47) + βCCN(11) + βCCC(16)
41	–	–	710.2412	29.3147	0.7356	βCCC(18) + γOCOC(17)
42	–	–	713.2248	74.2129	0.286	βCCC(11) + τCNCC(13) + τCCCC(12) + γOCOC(24)
43	–	698	720.76	34.4805	0.6079	τHCCC(11) + τOCHN(11) + τCCCC(21) + τCCCN(18)
44	–	–	764.8481	35.1287	1.355	τHCCC(20) + τHCCC(13) + τHCCC(35)
45	–	–	769.3558	86.099	0.5726	τHOCC(11) + τHCCC(14) + τCNCC(15)
46	–	754	772.5047	80.1123	1.5034	υNC(10) + τHNCC(29)
47	–	–	800.1705	32.614	9.5736	υCC(10) + τHOCC(45)
48	–	–	807.7648	33.1554	7.4711	υCC(12) + τHOCC(36)
49	–	–	834.9497	66.9488	6.744	υCC(14) + υNC(11)
50	818	–	842.467	11.3744	19.6	υCC(18) + υNC(20)
51	–	–	845.4772	22.2652	0.8552	τHCCC(13) + τHCCH(10) + τHCNC(15) + γOCOC(29) + γCCNC(17)
52	–	–	849.415	2.8528	0.5757	τHCCC(14) + τOCHN(11) + τOCCN(13) + γCNCC(29)
53	–	–	853.4054	3.8207	1.8783	τHCCN(14)
54	–	867	897.0902	1.0602	0.1917	βNCC(14) + βCCN(19) + τCNHC(11)
55	880	883	910.2819	9.818	3.3268	υNC(13) + υNC(17) + υNC(16) + υNC(10)
56	–	–	929.3588	0.6385	0.6884	τHCCC(32) + τHCCC(20) + τHCCC(14) + τHCCC(26)
57	–	907	931.5708	131.9479	6.5909	βOHO(51) + γOCOH(11)
58	–	–	942.8116	1.6197	0.27	τHCCC(49) + τHCCH(13) + τHCNC(19)
59	955	955	986.9852	0.2843	0.0966	τHCCC(13) + τHCCC(26) + τHCCC(44)
60	–	980	1013.7594	9.9235	30.7493	υNC(10) + υCC(11) + βCCC(31) + βCCC(15) + βCCN(14)
61	–	–	1020.6311	1.3719	0.255	υCC(12) + υNC(10) + βCCN(13) + βCCC(13) + τHCCC(63)
62	–	–	1020.8679	7.6813	23.6563	υCC(13) + βCCC(31) + τCCCC(15) + τHCNC(13)
63	–	–	1022.5986	0.1162	0.2223	τHCCC(23) + τHCCC(35) + τCCCC(22)
64	1001	1000	1032.6631	7.4644	4.3854	υCC(12) + βCNC(10)
65	–	–	1046.6492	8.4399	3.055	τHCCH(51) + τHCNC(14)
66	–	–	1057.6529	4.0541	2.1402	τNCCN(14)
67	–	–	1062.2869	7.9646	4.7683	υCC(13) + βCNC(13) + τHCNC(13)
68	–	–	1063.5794	13.2666	13.1589	υCC(10) + υCC(11) + βCNC(19)

(*continued on next page*)

Table 4 (*continued*)

S.No	FT-Raman	FT-IR	Theo. Freq.	IR Intensity	Raman Activity	Potential Energy Distribution (%)
69	–	–	1065.7114	11.7456	14.6638	υCC(27) + βHCC(11) + βCCC(12)
70	1047	1044	1072.9341	66.8137	6.5858	υCC(17) + βHCC(11)
71	–	1064	1093.8353	10.939	2.6876	υNC(37) + υNC(28)
72	1072	–	1108.6445	11.0336	4.1363	βHCC(10) + βHCC(12) + βHCC(13)
73	–	–	1109.8503	0.6053	1.8969	βHCC(13)
74	–	–	1131.0332	48.8147	0.8955	υOC(47) + βCCN(10)
75	1126	1124	1157.9993	23.3243	1.2751	υNC(37) + υNC(33)
76	–	–	1166.6278	1.9901	5.6263	υCC(16) + βHCC(19) + βHCC(26) + βHCC(29)
77	–	–	1170.9251	1.7392	7.053	υCC(17) + βHCC(29) + βHCC(13) + βHCC(29)
78	1152	1151	1185.3271	44.0613	6.911	υOC(10) + υCC(12) + βCNH(10) + βHCC(11) +
79	–	–	1187.9083	11.3628	6.3352	βHNC(12) + τCNCC(12)
80	–	1170	1207.8674	6.3588	8.6307	βHCN(18) + βHCC(12) + βHCN(28)
81	1202	–	1236.1663	2.8998	1.0748	βHCN(13) + βHCC(12) + τHCCN(13) + τHCNC(18)
82	–	–	1244.9605	21.1737	32.1923	υCC(14) + υNC(15) + υOC(10) + υCC(19) + βHOC(10)
83	–	1255	1290.3634	32.8227	4.6862	υNC(41) + υCC(11) + υNC(19)
84	–	–	1312.2906	4.4074	6.339	υNC(39)
85	–	–	1315.8188	1.6467	7.7225	υNC(14) + βHCC(10) + βHCC(30)
86	–	–	1317.834	19.4226	10.1817	βHCN(30) + βHCN(25)
87	1287	1295	1333.7034	8.3337	3.6035	υCC(13) + υNC(14) + βHCN(25)
88	–	–	1346.6771	0.6945	10.7363	βHCC(20) + βHCC(16) + τHCCN(12) + τHCCN(12)
89	1317	1318	1355.064	14.0166	3.4844	τHCNC(12) + τHCCN(18) + τHCNC(13)
90	–	–	1363.8892	24.2671	0.9029	τHCCN(18)
91	–	–	1407.7703	681.8668	63.6222	υOC(19) + υOC(40) + υCC(11)
92	–	–	1413.8055	20.7433	0.5461	βHCH(13) + τHCCN(12)
93	–	1380	1418.9769	441.7227	5.2974	βHOC(49)
94	–	–	1435.1217	1.7253	3.5017	τHCNC(22) + τHCNC(17)
95	–	1421	1459.8262	2.17	10.8562	βHCC(25) + βHCC(32)
96	1435	–	1477.8653	123.1001	4.955	βHCC(29) + βHOC(10) + βHCC(19)
97	–	1441	1485.0658	6.2384	3.2898	βHNC(42) + βHCH(11) + βHCH(11) + τHNCC(10)
98	–	–	1490.8379	9.9192	20.7195	βHCH(50) + βHCH(13)
99	–	–	1498.5267	10.6636	4.6721	υNC(16) + βHNC(13) + βHCC(12) + βHCH(23)
100	–	–	1498.8885	0.9609	5.6504	βHCC(27) + βHCH(11)
101	–	–	1503.2497	8.3919	0.9852	υNC(10) + βHCC(11) + βHCN(28) + βHCH(10)
102	–	1464	1505.4325	29.2151	4.5356	βHCH(21) + βHCH(22) + βHCH(17)
103	–	–	1510.8285	3.9242	6.3546	βHCH(17) + βHCH(19) + βHCH(23)
104	–	–	1534.8434	23.9643	3.5815	βCNH(17) + τCNHC(17)
105	–	–	1600.1086	557.0432	13.1206	υOC(27) + υOC(13)
106	–	1562	1612.0593	31.5291	0.8044	βCNH(15) + τHNHC(24)
107	–	–	1613.4844	11.9311	30.9222	υNC(16) + υCC(15) + υCC(33) + βHCC(11)
108	–	–	1621.1966	148.7222	24.9162	υOC(10) + υCC(23)
109	1582	1584	1631.8781	130.4448	24.6496	υOC(13) + υCC(12) + υCC(18)
110	–	–	1635.1038	40.7945	38.8431	υCC(32) + βCCC(14)
111	1625	1630	1683.2701	97.916	2.4268	τHOCO(10) + γOCOH(37)
112	–	–	1738.8253	207.1441	10.4067	βHNC(21) + τHOHN(14)
113	–	–	1845.6182	336.9096	53.495	υOC(83)
114	–	–	2122.8685	2953.74	144.6588	υNH(76)
115	2820	2824	2912.9275	63.3359	104.6549	υCH(96)
116	–	–	2927.6799	68.7217	141.8091	υCH(96)
117	2970	–	3066.0255	123.5579	176.8728	υNH(19) + υCH(40) + υCH(19)
118	–	–	3072.8245	20.9587	107.3046	υCH(41) + υCH(26)
119	–	–	3080.0086	105.1773	132.4527	υCH(77)
120	–	–	3084.8118	69.5875	110.7114	υCH(84)
121	3005	3005	3094.2853	428.3087	42.6018	υNH(20) + υCH(23) + υCH(21)
122	–	–	3127.3782	4.4177	42.7803	υCH(32) + υCH(53)
123	–	–	3130.3085	15.7402	74.0937	υCH(27) + υCH(56)
124	–	–	3138.0784	24.4073	86.5736	υCH(95)
125	3067	3067	3164.9825	125.9298	222.8386	υCH(91)
126	–	–	3168.8498	13.0604	107.1368	υCH(79) + υCH(18)
127	–	–	3175.7669	3.7238	105.3818	υCH(82)
128	–	–	3189.1779	32.379	242.6975	υCH(18) + υCH(78)
129	–	–	3198.1786	9.4653	143.3746	υCH(10) + υCH(85)
130	–	–	3211.8121	2.5114	133.5741	υCH(93)
131	–	–	3218.2148	2.0294	96.8089	υCH(97)
132	–	–	3223.183	1502.981	119.1839	υOH(95)
133	–	–	3509.882	206.8596	38.0278	υOH(99)
134	3441	–	3543.2857	1.9286	159.0257	υNH(100)
135	3759	–	3876.0272	47.6992	98.26	υOH(99)

υ-stretching, β-bending, γ-out of plane, τ-torsion

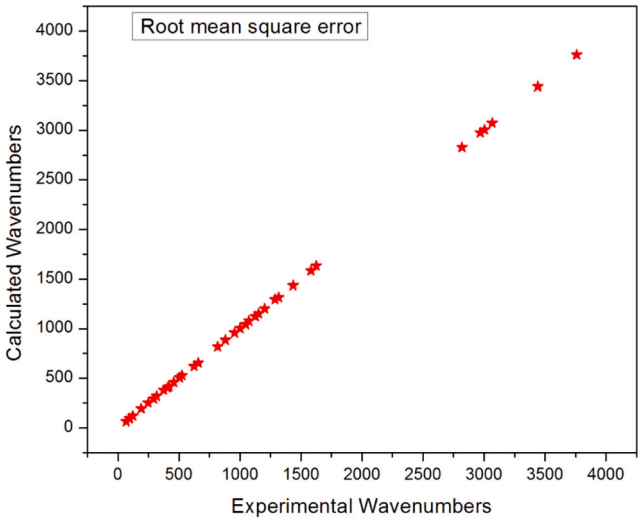

Fig. 9. Root Mean square error plot of PBCPM.

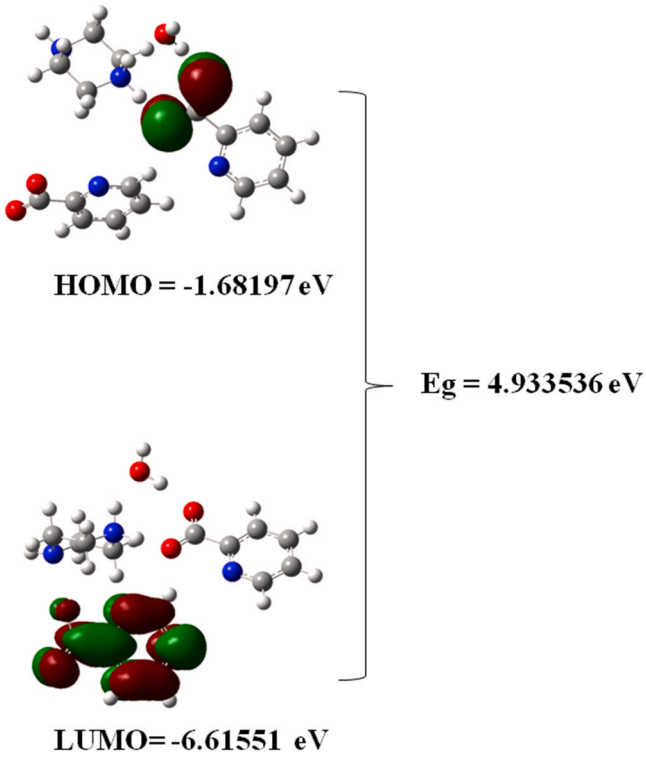

Fig. 10. HOMO LUMO Energy of PBCPM.

5.6. *Frontier molecular orbital*

The HOMO energies were determined to be 1.68197 eV, while the LUMO energies were calculated to be 6.61551 eV. The energy difference between the HOMO and LUMO not only determines molecular chemical equilibrium, but it also has an effect on molecular electrical transport properties. For the PBCPM molecule, the HOMO-LUMO energy gaps were found to be 4.933536 eV. According to the Koopmans theorem, the change in energy when an electron is removed from the system is referred to as Ionization potential, and it is equal to the highest occupied molecular orbital (HOMO) energy [33], while the change in energy when an electron is inserted into the system is referred to as Ionization potential, and it is equal to the lowest unoccupied molecular orbital (LUMO) energy. However, according to Kohn-Sham principle, the HOMO energy for a "n" electron system = IP and the –LUMO energy = EA when fine-tuning the

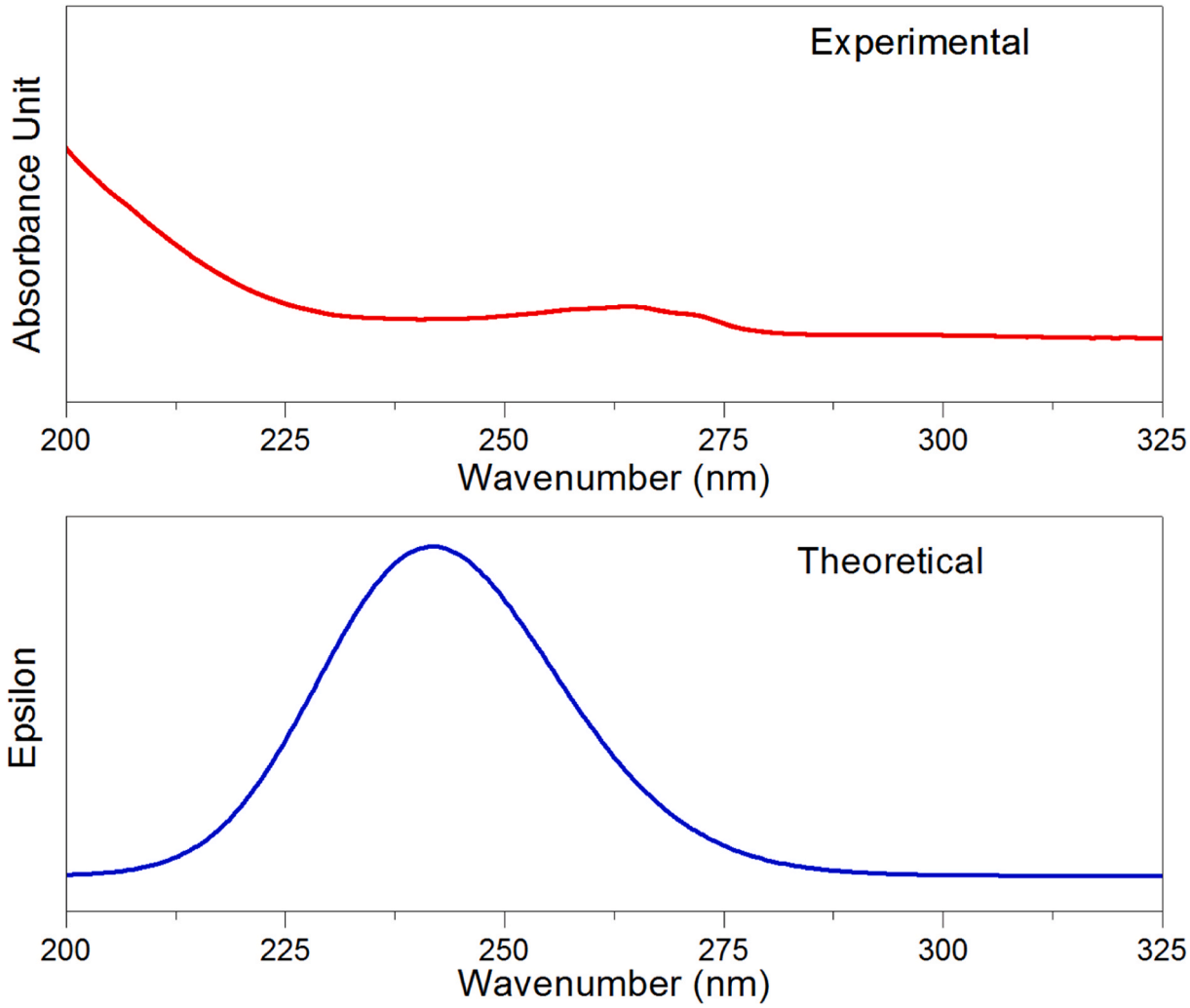

Fig. 11. Experimental and Theoretical UV-Vis spectrum of PBCPM.

energy bandgap. Using HOMO and LUMO powers, the terms of absolute hardness (η) and absolute electronegativity (χ) can be calculated [35,36]. For various structures, the value of correlates with chemical softness and hardness as measured empirically [37]. Ionization potential and electron affinity values are used to calculate critical quantities including global hardness, chemical potential, and global electrophilicity index. 2.46677 eV, 4.14874 eV, and 3.48879 eV are the prices. Fig. 10 depicts the HOMO-LUMO energy gap; this promising result shows the presence of nonlinear property in the synthesized crystal.

5.7. UV-vis spectroscopy

To illuminate the absorption spectroscopic nature of the PBCPM molecule, TD-DFT calculations were performed at the TD-B3LYP/6–311G range[28]. The PBCPM spectra were used to assess the accuracy of spectra measurement. The maximum absorption wavelengths, vertical excitation energies (E), and oscillator strengths (f), as well as the assignment of the electronic transitions in the PBCPM molecule, are addressed. Fig. 11 shows the experimental and measured UV-Vis absorption spectra of the title molecule. In the experimental UV-Vis spectrum in gas phase, the maximal excitation wavelengths are observed at 265 nm. The simulated absorption band for this wavelength is 241 nm (f = 0.5630). The measured values are considered to be in accordance with the experimental values. This short cut off wavelength value of PBCPM is an additional advantage of the production of third harmonics (NLO).

5.8. Molecular electrostatic potential

Molecular Electrostatic Potential Mapping (MEP) provides a wealth of information about a molecule's electronic and nuclear charge distribution, as well as a crucial tool for predicting and comprehending chemical reactivity. The most likely area of nucleophilic and electrophilic attack is determined by the Molecular Electrostatic Potential. The attractive potential is represented by a red region in

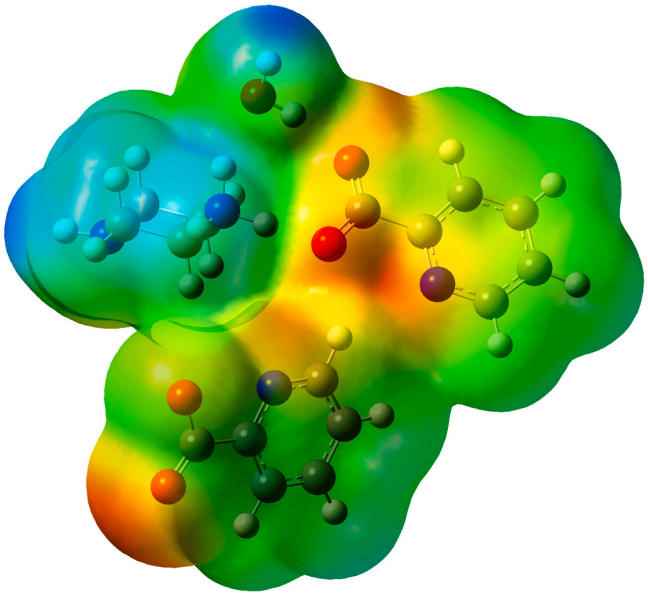

Fig. 12. Molecular Electrostatic Potential of PBCPM.

Table 5
Calculated Polarisability and Hyperpolarisability values of PBCPM.

Polarisability		Hyperpolarisability	
αxx	268.569	βxxx	143.673
αxy	9.337	βxxy	92.5568
αyy	222.076	βxyy	146.171
αxz	-7.233×	βyyy	29.54
αyz	-25.942	βxxz	7.2819
αzz	137.148	βxyz	-16.148
		βyyz	17.9122
		βxzz	31.4648
		βyzz	23.584
		βzzz	-27.824

MEP mapping, while the repulsive potential is represented by a blue region. The green area means that the electrostatic potential is negative. It qualitatively forecasts charge transfer phenomena based on colour transition. The PBCPM shows a strong red region at Oxygen, while the strength of the red region fades near the Carbon region of Picolinic acid, suggesting charge migration. The red component on MEP indicates electron attraction, so the PBCPM shows a strong red region at Oxygen. The extreme limits of the electron density observed in PBCPM are -6.438×10^{-2} (red) and $+ 6.438 \times 10^{-2}$ (blue); the output obtained depicts that the existence of nonlinear optical behavior present in the PBCPM[27]. The MEP of PBCPM is shown in Fig. 12.

5.9. Hyperpolarisability

The polarizability and hyperpolarizability of PBCPM were measured using the DFT-B3LYP method and 6–31 G(d,p) basis package, based on the finite-field approach, to investigate the relationships between photocurrent generation, molecular structures, and Non-Linear Optical property. Using x,y,z elements, the total static dipole moment (μ_0), the anisotropy of the polarizability ($|\alpha_0|$), mean polarizability ($\Delta\alpha$), and total first hyperpolarizability (β_0) are described.

$$\mu_0 = (\mu^2_x+\mu^2_y+\mu^2_z)^{1/2}$$

$$|\alpha_0| = 1/3(\alpha_{xx}+\alpha_{yy}+\alpha_{zz})$$

$$\Delta\alpha = 2^{-1/2}[(\alpha_{xx}-\alpha_{xx})^2+(\alpha_{yy}-\alpha_{zz})^2+(\alpha_{zz}-\alpha_{xx})^2]^{1/2}$$

$$\beta_0 = [(\beta_{xxx}+\beta_{xyy}+\beta_{xzz})^2+(\beta_{yyy}+\beta_{xxy}+\beta_{yzz})^2+(\beta_{zzz}+\beta_{xxz}+\beta_{yyz})^2]^{1/2}$$

Since the x, y, z components of α_0 and β_0 of Gaussian 09w output are reported in a atomic mass unit (a.u.), the calculated values have been converted into electrostatic unit (esu) using conversion factor as (for α_0: 1 a.u. = 0.1482×10^{-24} esu; for β_0: 1 a.u. =

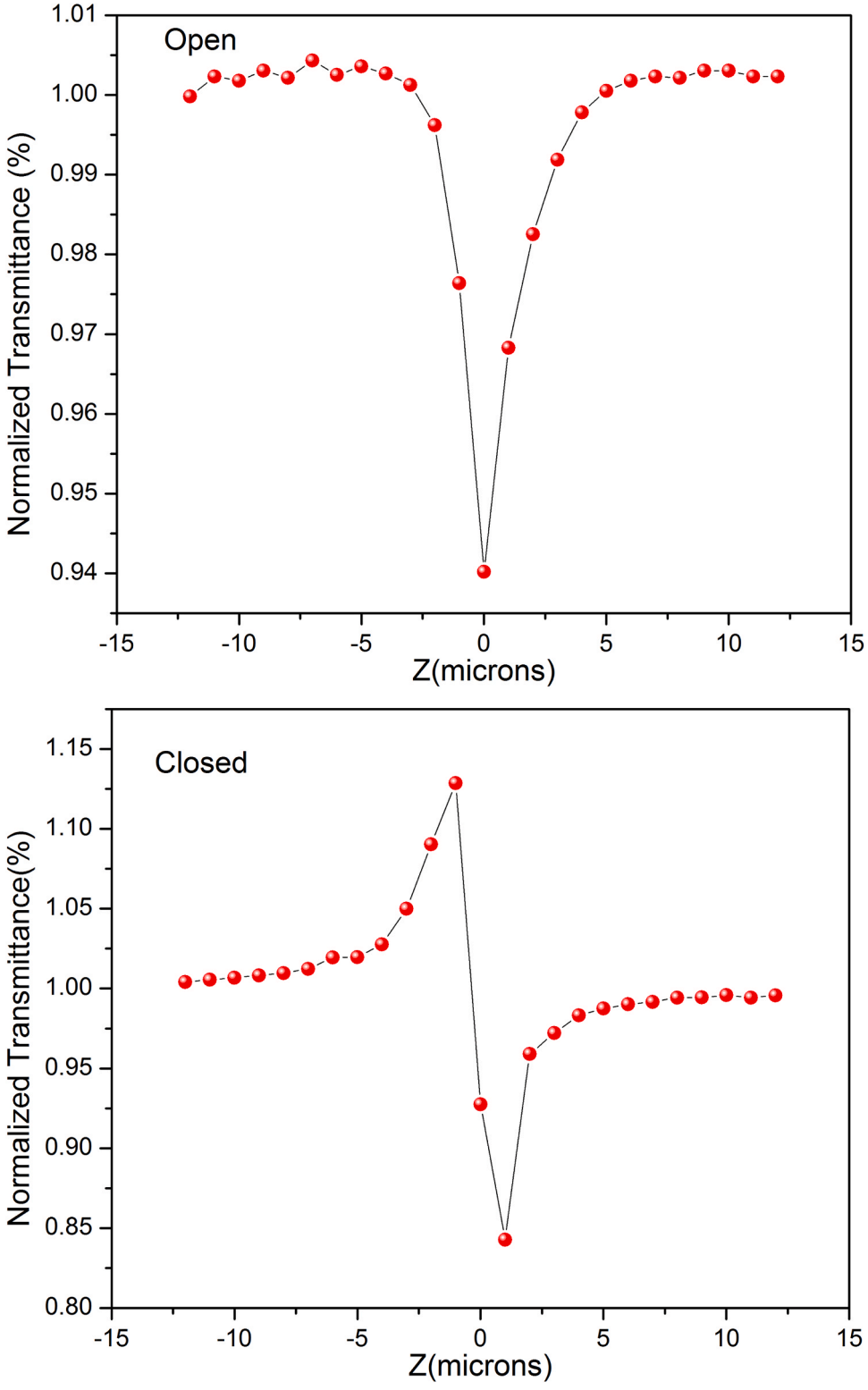

Fig. 13. a & b Open and closed aperture of PBCPM.

Table 6
Experimental Parameters used in Z-Scan Measurement.

Laser wavelength and power (Semiconductor – continuous wave laser)	532 nm and 100 mW
Optical Path length	733 mm
Beam radius at the aperture	3.5 mm
Radius of aperture	1.25 mm
Beam radius falling on the lens	3.1 mm
Sample Thickness	1 mm
Laser Power Io	8.57 kW/cm^{-2}
Focal length of lens	103 mm
Nonlinear refractive index (n^2)	3.17037×10^{-9} (m^2/W)
Nonlinear absorption coefficient (β)	2.4137×10^{-4} (m/W)
Real part of the third-order susceptibility [Re(χ^3)]	3.1139×10^{-6}
Imaginary part of the third-order susceptibility [Im(χ^3)]	2.5573×10^{-7}
Third-order nonlinear optical susceptibility (χ^3)	3.1243×10^{-6} esu

0.0086393 $\times10^{-30}$ esu). The α_0 and β_0 value of PBCPM 3.101301856 $\times$ 10^{-23} esu & 3.047962318 $\times$ 10^{-30} esu [27,28]. The calculated polarisability and hyperpolarizability value of PBCPM are shown in Table 5. The magnitude of β_0 is one of the key factors in an NLO system and the obtained result supports the suitability of PBCPM crystal in NLO applications.

5.10. Z-scan measurement

The Z-scan calculation is used to determine the third order nonlinear refraction index n2 and the nonlinear absorption coefficient of the PBCPM crystal. As a result, the NLO group quickly adopted the Z-scan approach as a standard technique for calculating nonlinear variations in optical absorption and changes in refractive index. A continuous wave He-Ne laser with a wavelength of 532 nm was used in our experiments. The following are the specifics of the estimate. The sign of the non linear phase shift φ determines the direction of the peak and valley in relation to the z-axis. The difference in normalised transmittance between the peak and valley can be used to calculate the amplitude of the phase change [34–37].

$$\Delta T_{p-v} = 0.406(1-S)^{0.25} \mid \varphi \mid \tag{1}$$

where S is the aperture linear transmittance and is calculated using the following equation

$$S = 1\text{–}exp\left(-2{r_a}^2/{\omega_a}^2\right) \tag{2}$$

where r_a is the radius of the aperture and ω_a is the beam radius at the aperture, the non-linear refractive index is given by the relation

$$n_2 = \varphi / KI_0L_{eff} \tag{3}$$

where, K = 2π/λ (where λ is the laser wavelength).

I_0 is the input intensity, (Z = 0, L_{eff}=[1 – exp(–α L)]/α is the effective thickness of the sample and $\alpha$is the linear absorption co-efficient of the PBCPM crystal. The non-linear absorption co-efficient is calculated from the open aperture Z-scan data as

$$\beta = 2\sqrt{2}\Delta T \Big/ I0Leff \tag{4}$$

Where,ΔT is the one valley at the open aperture Z-scan curve.

For saturable absorption, the value of will be negative, but for two photon absorption, it will be positive. Equation χ^3 defines the true and imaginary components of the third order non-linear optical susceptibility.

$$Re\chi^3(esu) = 10^{-4}\left(\varepsilon_0 C^2 {n_0}^2 n_2\right)/\pi \ \ \left(Cm^2/W\right) \tag{5}$$

$$Im\chi^3(esu) = 10^{-2}\left(\varepsilon_0 C^2 {n_0}^2 \lambda\beta\right)/4\pi^2 \ (Cm/W) \tag{6}$$

where ε_0 is the vacuum permittivity, n_0 is the sample's linear refractive index, and C is the light's velocity in vacuum. Fig. 13a and b display the open and closed apertures of the PBCPM crystal. Table 6 lists the experimental parameters used in Z-scan measurement. In our experiment for PBCPM crystal non linear refractive index $n_2 = 3.17 \times 10^{-9}$($m^2$/W). The absorption co-efficient β calculated from open aperture normalized transmittance was obtained to $\beta = 2.41 \times 10^{-4}$(m/W). According to the equation be (5) & (6), this value of n_2 and β can be used to calculate χ^3. The third-order nonlinear optical susceptibility $\chi^3 = 3.12 \times 10^{-6}$ esu. This positive third order nonlinear optical response of the PBCPM crystal leads the way for further research in the field of fabricating NLO device.

6. Conclusion

Using experimental techniques such as X-ray diffraction, FT-IR, FT-Raman, and UV–Vis absorption spectra, the structural,

vibrational, mechanical, and NLO properties of PBCPM are recorded. When the solid-state crystal structure was compared to the optimised structure in the gas phase DFT/B3LYP/6–311G (d,p), no major geometrical deviations (distances and angles) were found. The Hirshfeld Surface Analysis exemplifies the technique's ability to map out interactions. The Spectroscopy study reveals that the principal vibrational frequencies determined from the optimised structure and the experimental spectroscopic results agree very well. The negative potential sites are as and the electronegative atoms, while the positive potential sites are around the hydrogen atoms, according to the MEP diagram. The PBCPM's hyperpolarizability values are calculated, which resembles the molecule's Non Linear Optical nature. The nonlinear optical refractive index n_2 ($3.17 \times 10^{-9}(m^2/W)$), nonlinear absorption coefficient β ($2.41 \times 10^{-6}(m/W)$) were calculated by Z-scan technique. Thus, PBCPM crystal could be a promising material for fabricating solid state NLO device.

Declaration of Competing Interest

The authors declare that the research article has no known conflict of interest.

Appendix A. Supporting information

Supplementary data associated with this article can be found in the online version at doi:10.1016/j.ijleo.2021.167836.

References

[1] D. Wang, G. Zhou, X. Xu, Wang, H. Liu, Y. Ren, Z. Shao, M. Jiang, Actively Q-switched intracavity second-harmonic generation of in BiB3O6 crystal, Opt. Laser Technol. 34 (2002) 343–346.
[2] M.H. Jiang, Q. Fang, Organic and semiorganic nonlinear optical materials, Adv. Mater. 11 (1999) 1147–1151.
[3] J. Badan, R. Hierle, A. Perigaud, J. Zuss (Eds.), Non-linear Optical Properties of Organic Molecules and Polymeric Materials, American Chemical Symposium Series 233, American Chemical Society, Washington, DC, 1993.
[4] M.D. Aggarwal, J. Choi, W.S. Wang, K. Bhat, R.B. Lal, A.D. Shields, B.G. Penn, D.V. Frazier, J. Cryst. Growth 179 (1999) 2004.
[5] J. Zyss, N.F. Nicoud, M.J. Coquillay, Chirality and hydrogen bonding in molecular crystals for phase-matched second-harmonic generation: N-(4–nitrophenyl)-(L)-prolinol (NPP), Chem. Phys. 81 (1984) 4160–4167.
[6] I. Ledoux, J. Badan, J. Zyss, A. Migus, D. Hulin, J. Etchepare, G. Grillon, A.J. Antonetti, Generation of high-peak-power tunable infrared femtosecond pulses in an organic crystal: application to time resolution of weak infrared signals, J. Opt. Soc. Am. B 4 (1987) 987–997.
[7] M. Thangaraj, G. Ravi, T.C. Sabari, Girisun, ethylenediaminium di(2-nitrophenolate) single crystals as materials for optical second harmonic generation, Phys. B Condens. Matter 449 (2014) 209–213.
[8] T. Ishihara, K. Koshino, H. Nakashima, Second harmonic generation due to quadrupole interaction in a photonic crystal slab: angle dependence and symmetry of the unit cell, Phys. Rev. Lett. 91 (2003) 253901–253911.
[9] G. Lüpke, D.J. Bottomley, H.M. Van Drile, Second- and third-harmonic generation from cubic centrosymmtric crystal with vicsssinal faces: phenomenological theory and experiment, J. Opt. Soc. Am. B 11 (1994) 33–43.
[10] Seth R. Marder, Joseph W. Perry, William P. Schaefer, Synthesis of organic salts with large second-order optical nonlinearities, Science 245 (1989) 626–628.
[11] D.J. Conrado, H. Verli, G. Neves, C.A. Fraga, E.J. Barreiro, S.M. Rates, T. Dalla- Costa, Pharmacokinetic evaluation of LASSBio-579: an N-phenylpiperazine antipsychotic prototype, J. Pharm. Pharmacol. 60 (2008) 699–707.
[12] A. Parkin, I.D.H. Oswald, S. Parsons, Structures of piperazine, piperidine and morpholine, Acta Crystallogr. Sect. B Struct. Sci. B60 (2004) 219–227.
[13] D. Havliček, J. Plocek, I. Němec, R. Gyepes, Z. Mička, The crystal structure, vibrational spectra, and thermal behavior of piperazinium(2+) selenate monohydrate and n, n′-dimethylpiperazinium(2+) selenate dihydrate, J. Solid State Chem. 150 (2000) 305–315.
[14] D. Havliček, V. Chudoba, I. Němec, I. Císařová, Z. Mička, Preparation, crystal structure, vibrational spectra and thermal behaviour of piperazinium(2+) selenite monohydrate and piperazinium(2+) diselenite, J. Mol. Struct. 606 (2002) 101–116.
[15] J. Plocek, D. Havliček, I. Němec, I. Císařová, Z. Mička, The crystal structure, vibrational spectra, and thermal behavior of dilithium piperazinium(2+) selenate tetrahydrate and dilithium N,N′-dimethylpiperazinium(2+) selenate tetrahydrate, J. Solid State Chem. 170 (2003) 308–319.
[16] V. Subhashini, S. Ponnusamy, C. Muthamizhchelvan, B. Dhanalakshmi, Growth and characterization of piperazinium 4-nitrophenolate monohydrate (PNP): a third order nonlinear optical material, Opt. Mater. 35 (7) (2013) 1327–1334.
[17] V. Subhashini, S. Ponnusamy, C. Muthamizhchelvan, Synthesis, growth, spectral, thermal, mechanical and optical properties of piperazinium (meso)tartrate crystal: a third order nonlinear optical material, J. Cryst. Growth 363 (2013) 211–219.
[18] S. Gowri, T. Uma Devi, S. Alen, D. Sajan, C. Surendra Dilip, G. Vinitha, J. Mater. Sci. Mater. Electron. 29 (2018) 19710–19723.
[19] S. Gowri, T. Uma Devi, D. Sajan, C. Surendra Dilip, A. Chandramohan, N. Lawrence, Crystal growth, spectral, optical and thermal properties of semiorganic nonlinear optical material: picolinic acid hydrochloride, Spectrochim. Acta Part A Mol. Biomol. Spectrosc. 110 (2013) 28–35.
[20] A.T. Ravichandran, R. Rathika, M. Kumaresavanji, Growth and Z-scan analysis of semi-organic Bis(picolinic acetate) Zinc(II) single crystal for third order NLO applications, J. Mol. Struct. 1224 (2021), 129048.
[21] SAINT Plus (v 6.14); Bruker AXS Inc.: Madison, WI, 2008.
[22] G.M. Sheldrick, A short history of SHELX, Acta Crystallogr. A 64 (2008) 112–122.
[23] G.M. Sheldrick, Crystal structure refinement with SHELXL, Acta Crystallogr. C 71 (2015) 3–8.
[24] A.L. Spek, PLATON, A Multipurpose Crystallographic Tool; Utrecht University: Utrecht, Netherland, 2002.
[25] A.L. Spek, Single-crystal structure validation with the program PLATON, J. Appl. Crystallogr. 36 (2003) 7–13.
[26] S.K. Wolff, D.J. Grimwood, J.J. McKinnon, D. Jayatilaka, M.A. Spackman, CrystalExplorer1.5. University of Western Australia 2005, http://www.Theochem.uwa.edu.au/crystal_explorer/.
[27] H.B. Schlegel, Optimization of equilibrium geometries and transition structures, J. Comput. Chem. 3 (1982) 214–218.
[28] M.J. Frisch, et al., Gaussian-09, Revision A.01, Gaussian, Inc., Wallingford, CT, 2009.
[29] R. Dennington, T. Keith, J. Millam, GaussView, Version 5, Semichem Inc., Shawnee Mission, KS, 2009.
[30] J.J. Mckinnon, P.A.F. Fabbiani, M.A. Spackman, Comparison of polymorphic molecular crystal structures through Hirshfeld surface analysis, Cryst. Growth Des. 7 (2007) 755–769.
[31] M.A. Spackman, D. Jayatilaka, Hirshfeld surface analysis, Cryst. Eng. Comm. 11 (2009) 19–32.
[32] M.P. Andersson, P. Uvdal, New scale factors for harmonic vibrational frequencies using the B3LYP density functional method with the triple-ú basis set 6-311+G (d,p), J. Phys. Chem. A 109 (2005) 2937–2941.
[33] J. Cooper, J. Zhang, C. Grant, Ab initio calculation of ionization potential and electron affinity of six common explosive compounds, Rep. Theor. Chem. (2012) 11, https://doi.org/10.2147/rtc.s36686.

[34] R.G. Parr, L.V. Szentpály, S. Liu, Electrophilicity index, J. Am. Chem. Soc. 121 (1999) 1922–1924, https://doi.org/10.1021/ja983494x.
[35] R.G. Parr, R.A. Donnelly, M. Levy, W.E. Palke, Electronegativity: the density functional viewpoint, J. Chem. Phys. 68 (8) (. 1978) 3801–3807.
[36] R.G. Parr, R.G. Pearson, Absolute hardness: companion parameter to absolute electronegativity, J. Am. Chem. SOC 105 (1983) 7512–7516.
[37] R. Pearson, Hard and soft acids and bases, J. Am. Chem. Soc. 85 (1963) 3533–3539.